Research Square

Preprints are preliminary reports that have not undergone peer review.
They should not be considered conclusive, used to inform clinical practice,
or referenced by the media as validated information.

Integrated transcriptomics reveal CTHRC1-associated immune resistance and JAM2– F11R–STAT1 macrophage remodeling in anaplastic thyroid carcinoma

Xiaoting Wang[1]
China-Japan Friendship Hospital
Bo Zhang[2]
thyroidus@163.com

China-Japan Friendship Hospital
Ke Yang[1]
China-Japan Friendship Hospital
Peitong Deng[1]
China-Japan Friendship Hospital

Research Article

Keywords: anaplastic thyroid carcinoma, CTHRC1, macrophage state remodeling, tumor microenvironment, spatial transcriptomics, immune therapy

Posted Date: September 24th, 2026

DOI: https://doi.org/10.21203/rs.3.rs-10904032/v1

License: This work is licensed under a Creative Commons Attribution 4.0 International License.
Read Full License

Additional Declarations: No competing interests reported.

Abstract

Background

Anaplastic thyroid carcinoma (ATC) is a rare but highly lethal thyroid malignancy. Immune checkpoint blockade (ICB) has shown therapeutic activity in ATC, but responses remain limited and heterogeneous. The immune microenvironment underlying ICB resistance in ATC remains incompletely characterized, highlighting the need to identify biologically relevant biomarkers and therapeutic vulnerabilities.

Methods

We integrated multiple ATC bulk transcriptomic cohorts with single-cell and spatial transcriptomic datasets and two pretreatment ICB cohorts. Candidate genes were prioritized across ATC progression and ICB nonresponse, followed by single-cell and spatial characterization, myeloid state reconstruction, ligand–receptor analysis, and in silico perturbation.

Results

Integrated analysis prioritized CTHRC1 as a candidate linking ATC progression with ICB nonresponse and confirmed its consistent upregulation in ATC. Single-cell analysis localized CTHRC1 mainly to malignant epithelial, fibroblast/CAF, and endothelial compartments and showed that CTHRC1-positive malignant cells exhibited a broader resistance-associated transcriptional state. Spatial analysis identified focal CTHRC1-high immune resistance niches containing CAF, M2-like macrophage, CD8/cytotoxic, and T-cell exhaustion signals. Myeloid analysis revealed a reproducible S100A12-positive monocyte–SPP1-positive TAM–ADAMDEC1-associated macrophage continuum, with STAT1 as the leading transition-associated regulator. Receiver state-guided communication analysis prioritized JAM2–F11R as the top malignant-to-myeloid interaction, supported by F11R/STAT1 perturbation, independent single-cell replication, and spatial coupling. The integrated CTHRC1-related feature was associated with ICB nonresponse, while virtual CTHRC1 knockout predicted reductions in multiple resistance-related programs.

Conclusions

The CTHRC1-associated immune resistance niche is linked to ICB nonresponse in ATC, while JAM2–F11R–STAT1 may contribute to ADAMDEC1-associated macrophage state remodeling, suggesting CTHRC1 as a potential therapeutic target to improve immunotherapy responsiveness in ATC.

Background

Anaplastic thyroid carcinoma (ATC) is uncommon but remains one of the most lethal thyroid malignancies [1, 2]. Targeted therapy has changed the outlook for selected molecular subgroups, especially BRAF V600E-mutant disease [3]. Immune checkpoint blockade (ICB) has produced responses in ATC [4, 5], including in recent combination studies [6, 7], but benefit remains uneven and often short-lived. The unresolved problem is therefore not whether ATC is immunologically active, but why an immune-infiltrated tumor microenvironment fails to generate effective antitumor immunity. TGF-β-driven extracellular matrix (ECM) programs can limit T-cell infiltration and contribute to checkpoint resistance [8, 9]. Related cancer-associated fibroblast (CAF) states have been linked to immunotherapy resistance [10, 11] and CD8 + T-cell exclusion [12, 13]. CAF–macrophage interactions can reinforce suppressive myeloid states [14], while FAK signaling links stromal remodeling to reduced cytotoxic T-cell infiltration [15]. These observations argue against a purely checkpoint-centered view of resistance.

ATC studies have described molecular and tumor microenvironment subtypes [16], genomic and evolutionary changes [17], inflammatory and mesenchymal malignant cell states [18], macrophage-rich immunosuppressive microenvironments [19, 20], and dysfunctional or pre-exhausted T cells [21]. Spatial studies revealed tumor–stroma organization [22, 23] and ATC-associated molecular features [24]; ECM remodeling has also been implicated [25, 26]. How these features connect remains unclear, including whether malignant, stromal, and myeloid programs occupy one niche and which malignant cell signal links to macrophage remodeling.

We approached this question by first prioritizing genes associated with both ATC progression and ICB nonresponse, and then tracing the leading candidate across single-cell and spatial datasets. CTHRC1 emerged as the top candidate. We then asked which cell populations express CTHRC1, whether CTHRC1-high regions define a coherent multicellular niche, and whether a specific malignant-to-myeloid signaling axis is associated with the macrophage state within that niche.

This strategy allowed us to move from a candidate gene to the organization of the local tumor microenvironment, and then to a defined macrophage remodeling program. We further examined whether the broader CTHRC1-associated state was related to ICB response and whether its resistance-related programs were altered by computational perturbation.

Methods

Study design and data sources

Public datasets were used throughout. Bulk ATC cohorts were GSE29265, GSE33630, GSE53072, GSE65144 and GSE76039, with GSE9115 and GSE27155 used for additional comparisons. Single-cell analyses used GSE193581 [18] and GSE232237 [29]. Four ATC Visium sections from GSE250521 [22] provided spatial data. Pretreatment ICB analyses used GSE78220 [27] and GSE91061 [28], both melanoma cohorts. GSE248058 [30] and GSE211806 [31] were used for orthogonal FAK- and TGF-β-related perturbation analyses.

Identification of ATC progression-associated genes and construction of the AICR program

Each bulk dataset was normalized and analyzed with limma [32]. ATC was compared with normal thyroid, papillary thyroid carcinoma (PTC) and poorly differentiated thyroid carcinoma (PDTC). Progression-associated genes required a positive pooled effect, concordant direction in at least two-thirds of comparisons and meta-analysis FDR < 0.05. ICB nonresponse-associated genes required a positive pooled effect and meta-analysis FDR < 0.10. Genes supported by both analyses formed the ATC-associated immune checkpoint resistance (AICR) candidate set. The top 100 genes defined the AICR program, and candidates were ranked with ATC effect, cross-cohort consistency, ICB evidence, single-cell source and spatial/stromal evidence.

Single-cell processing and stratification of malignant cells by CTHRC1 expression

GSE193581 and GSE232237 were processed separately with Seurat [33] for quality control, normalization, dimensionality reduction, and clustering. Doublets were assessed and cell types annotated before downstream analysis. After filtering, GSE193581 contained 33,936 cells from nine ATC samples; GSE232237 contained 84,804 cells from five ATC and seven PTC samples. Malignant/epithelial cells were annotated using epithelial and thyroid lineage markers together with tumor-associated expression patterns.

For cell-level stratification, malignant/epithelial cells with normalized CTHRC1 expression > 0 were classified as CTHRC1-positive, whereas cells with CTHRC1 expression = 0 were classified as CTHRC1-negative. Comparisons between the two groups were performed within individual samples, and patient-level effect estimates rather than pooled cell counts were used for cross-sample statistical summaries.

Construction and scoring of the CTHRC1-independent resistance program

Normalized single-cell expression was ln[1 + 10,000 × (gene count/total UMI count)]. The integrated resistance program contained nine prespecified modules: AICR, ECM remodeling, EMT, CAF, myCAF, TGF-β, myeloid suppression, checkpoint ligands and T-cell exhaustion. CTHRC1 was removed from the AICR set for CTHRC1-stratified analyses, leaving a fixed 99-gene AICR signature. Module scores were means of normalized constituent gene expression; myeloid suppression was the mean of TAM and M2-like TAM scores.

Module scores were z-standardized within each dataset and averaged with equal weight to form a CTHRC1-independent integrated resistance score. Patient-level analysis required at least 10 CTHRC1-

positive and 20 CTHRC1-negative malignant/epithelial cells. The effect for each patient was the median score in CTHRC1-positive cells minus the median score in CTHRC1-negative cells.

Spatial transcriptomic and neighborhood analyses

The four GSE250521 ATC Visium sections were processed separately. Tissue-covered spots with valid transcript detection were retained and aligned to the corresponding H&E images. Within each section, CTHRC1-high spots were defined as detectable CTHRC1 expression above the section-specific 75th percentile; the remaining tissue spots formed the reference group.

Spatial AICR used the fixed CTHRC1-excluded 99-gene signature. The CTHRC1-independent spatial resistance core combined AICR99, ECM/invasion, TGF-β, CAF, M2-like TAM, checkpoint ligand, T-cell exhaustion and FAK/SRC modules after within-section z-standardization. A separate integrated spatial score also included CTHRC1 and was used only for visualization.

Within each section we calculated Spearman correlation between CTHRC1 and the resistance core, and the core score difference between CTHRC1-high and reference spots. First- and second-order Visium neighborhoods were tested by label permutation. Spatial lag and bivariate Moran analyses were used for local association. Section-level effects were combined by signed Stouffer analysis, with Benjamini–Hochberg correction within each comparison family.

Myeloid state reconstruction, trajectory analysis, and regulon prioritization

Myeloid cells were reanalyzed separately in both single-cell datasets. S100A12-positive monocytes, SPP1-positive TAMs and ADAMDEC1-associated macrophages were identified from marker profiles. Patient-level pseudobulk expression for ADAMDEC1-associated and S100A12-associated populations was compared across datasets by effect correlation, directional concordance and concordant FDR-supported genes; ranked pathway enrichment used the same cross-dataset differential expression results.

Pseudotime was reconstructed across the S100A12-positive monocyte, SPP1-positive TAM and ADAMDEC1-associated macrophage continuum. Genes varying along scaled pseudotime defined the transition program. Transcription factor regulons were ranked by agreement with that program, target gene support and sample consistency. The resulting STAT1-associated transition program and ADAMDEC1 state were then used as receiver features for communication analysis.

Cell–cell communication analysis and state-first ligand–receptor prioritization

Communication prioritization combined malignant ligand and receiver receptor expression with NicheNet ligand–target relationships [34] and spatial association, consistent with spatially informed communication frameworks [35]. Broader pathway-level results were analyzed separately.

For the focused myeloid analysis, ligand–receptor pairs were ranked against the predefined STAT1 transition and ADAMDEC1 receiver state features. Ranking incorporated malignant ligand expression, myeloid receptor expression and association with the receiver programs. The highest-ranked pairs were carried into perturbation and spatial analyses.

Targeted in silico perturbation and spatial validation

F11R and STAT1 knockout and overexpression were modeled in sample-specific signed regulatory networks. Readouts were the STAT1 regulon, STAT1 transition program, ADAMDEC1 state, terminal state markers and root state markers. Directional consistency was checked across individual networks and by leave-one-sample-out analysis.

The STAT1 transition program was independently assessed in GSE193581 and GSE232237 as a late-minus-early trajectory signal. For spatial testing, the CTHRC1/JAM2 sender score, F11R expression, STAT1 transition score and ADAMDEC1 state score were mapped to Visium coordinates. Consecutive links in this chain were tested with coordinate shift null models within each section and combined across the four sections with multiple testing correction.

Public ICB treatment response analysis

Pretreatment samples from GSE78220 (n = 27; 15 responders and 12 nonresponders) and GSE91061 (n = 49; 10 responders and 39 nonresponders) were included. Complete response and partial response were classified as response, whereas stable disease and progressive disease were classified as nonresponse. The analysis included CTHRC1, AICR, EMT/ECM, CTHRC1 reversal burden, and FAK/SRC.

Each feature was z-standardized within cohort. The integrated ICB feature score was calculated as the unweighted mean of the five standardized features:

Integrated ICB feature score = [z(CTHRC1) + z(AICR) + z(EMT/ECM) + z(reversal burden) + z(FAK/SRC)] / 5.

Associations with ICB nonresponse were evaluated using cohort-adjusted logistic regression for the integrated score and each individual feature:

$\text{logit}[P(\text{nonresponse})] = \beta 0 + \beta 1 z(\text{feature}) + \beta 2 I(\text{GSE91061})$.

Odds ratios represent the change in the odds of nonresponse per 1-SD increase in a within-cohort standardized feature. Odds ratios with Wald 95% confidence intervals were reported. Statistical

significance was assessed using one-degree-of-freedom likelihood ratio tests comparing each feature model with the cohort-only model, followed by Benjamini–Hochberg correction across the six models.

Pretreatment feature distributions were summarized descriptively. ROC analyses were performed separately in GSE78220 and GSE91061 for the integrated ICB feature score and standardized CTHRC1, with nonresponse defined as the positive class. AUC 95% confidence intervals were estimated from 2,000 response-stratified, sample-level bootstrap resamples. Because these cohorts contributed to the development of the ICB nonresponse framework, ROC results were interpreted as within-cohort discrimination.

Virtual CTHRC1 perturbation and external perturbation analyses

Virtual CTHRC1 knockout was run with scTenifoldKnk [36] in five GSE193581 malignant cell networks (ATC08, ATC09, ATC11, ATC12 and ATC13). Absolute gene-level Z statistics were converted to within-network percentile ranks. Direction was assigned from an independent CTHRC1 coexpression consensus; CTHRC1 itself was removed before module projection. Signed gene values were summarized by the median for each module.

AICR, ECM remodeling, EMT, TAM recruitment, T-cell exclusion, TGF-β, CAF activation, myCAF and antigen presentation were assessed. The main figure displays the eight resistance-oriented modules, for which a negative value represents movement away from the CTHRC1-associated state. Module-level inference used one-sided exact Wilcoxon signed-rank tests with Benjamini–Hochberg correction.

For orthogonal perturbation support, GSE248058 [30] compared 24-h VS4718 FAK inhibition with vehicle in mouse KP2 pancreatic ductal adenocarcinoma organoids; FAK–SRC and EMT–ECM scores and gene-level changes were examined. GSE211806 [31] tested TGF-β induction and galunisertib rescue in PLC/PRF/5 and SNU-449 hepatocellular carcinoma cells at both program and gene levels. Program-level tests used exact permutation procedures with Benjamini–Hochberg correction.

Statistical analysis

All statistical tests were two-sided unless otherwise specified. The unit of statistical inference was defined according to the biological level of each analysis: individual patients or biological samples for cohort-level and single-cell analyses, tissue sections for cross-section spatial analyses, and sample-specific networks for virtual perturbation analyses. Cell- and spot-level measurements were summarized or permuted within their corresponding biological units rather than treated as independent replicates.

Effect sizes, medians, 95% confidence intervals, and multiplicity-adjusted P values were reported as appropriate for each analysis. Benjamini–Hochberg correction was applied where multiple hypotheses were tested within the same analysis.

Results

Multi-cohort integration prioritizes CTHRC1 across ATC progression and ICB nonresponse

We first identified transcriptional features shared between ATC progression and ICB nonresponse. ATC versus normal, ATC versus PTC, and ATC versus PDTC contrasts from multiple bulk transcriptomic cohorts were integrated with two pretreatment melanoma ICB cohorts (Fig. 1a). Genes showing concordant positive associations with both ATC progression and ICB nonresponse were used to define the ATC-associated immune checkpoint resistance (AICR) program. In the two thyroid comparison cohorts, AICR scores were highest in ATC, with lower levels in PTC and normal thyroid tissue (Fig. 1d).

CTHRC1 was strongly upregulated in ATC. In GSE33630, CTHRC1 expression was higher in ATC than in normal thyroid tissue (log2FC = 4.60, FDR = 5.40 × 10^-26; Fig. 1b), with positive effects across the other evaluable ATC progression-related contrasts (Fig. 1c). CTHRC1 ranked 11th among genes in the AICR program. Candidate prioritization was then extended to additional evidence from malignant cell specificity, stromal/ECM association, single-cell expression, and spatial analyses (Fig. 1e–h). CTHRC1 achieved the highest overall target score and was selected for subsequent single-cell and spatial analyses.

CTHRC1 is concentrated in malignant/epithelial and stromal compartments

Single-cell analysis showed a nonuniform distribution of CTHRC1 across cell populations (Fig. 2a, b). In GSE193581 ATC, the median CTHRC1-positive fractions were highest in fibroblasts/CAFs (79.3%), malignant/epithelial cells (65.4%), and endothelial cells (54.3%), whereas CTHRC1-positive fractions remained low in the major immune populations (0.6%–3.3%). A similar compartmental pattern was observed in GSE232237 ATC, with median CTHRC1-positive fractions of 40.0% in fibroblasts/CAFs, 36.5% in endothelial cells, and 30.1% in malignant/epithelial cells.

Within-patient comparisons showed higher CTHRC1-positive fractions and higher median AICR scores in malignant/epithelial cells than in the remaining cell populations (Fig. 2c). The cellular composition of the CTHRC1-positive pool differed across GSE193581 ATC, GSE232237 ATC, and GSE232237 PTC (Fig. 2d). At the patient level, tumor/stromal source summaries were higher than immune/other source summaries in all three groups (FDR = 0.014, 0.030, and 0.017, respectively; Fig. 2e). The patient-level heatmap showed marked interpatient variation in the distribution of CTHRC1-positive cells across malignant/epithelial, fibroblast/CAF, and endothelial compartments, while CTHRC1 remained low in most immune populations (Fig. 2f).

(e) Within-patient comparison of tumor/stromal and immune/other CTHRC1 source summaries across the three groups. (f) Patient-level heatmap of CTHRC1-positive fractions across major cell populations; gray indicates non-evaluable combinations.

CTHRC1-positive malignant cells exhibit a broader resistance-associated transcriptional state

We next examined whether CTHRC1 expression was associated with a broader resistance-related malignant cell state. In within-patient comparisons, the CTHRC1-independent integrated resistance score was higher in CTHRC1-positive malignant/epithelial cells, with median positive-minus-negative differences of 0.478 in GSE193581 and 0.098 in GSE232237. Positive shifts were observed in 5/5 evaluable patients in GSE193581 and 4/5 in GSE232237, although the integrated score did not remain significant after multiple testing correction (FDR = 0.0625 in both datasets; Fig. 3b). The CTHRC1-excluded AICR score showed a more consistent increase, with positive shifts in all five evaluable patients in both datasets and median differences of 0.176 and 0.015, respectively (FDR = 0.03125 in both datasets; Fig. 3a, c).

Resistance-related programs showed broadly concordant changes between CTHRC1-positive and CTHRC1-negative malignant/epithelial cells. AICR, ECM/EMT, CAF-related, TGF-β, checkpoint, and T-cell exhaustion programs generally shifted in the positive direction in both datasets, although effect sizes were larger in GSE193581 (Fig. 3a, c, d). Patient-level pseudobulk profiles showed substantial interpatient heterogeneity in these transcriptional programs (Fig. 3e), while single-cell activity maps showed partial overlap between CTHRC1 expression and individual resistance-related programs (Fig. 3f). CTHRC1 positivity therefore marked a broader resistance-associated malignant cell state with considerable heterogeneity across tumors.

(f) Representative single-cell activity maps of CTHRC1 and selected resistance-related programs. CTHRC1 was excluded from the AICR and integrated resistance scores used for CTHRC1 state comparisons. Color scales in panel F are specific to each transcriptional program.

CTHRC1-high spatial regions define focal resistance niches with stromal, myeloid, and T-cell remodeling

Spatial analysis of four ATC sections from GSE250521, comprising 11,622 tissue-covered spots, showed marked intratumoral heterogeneity (Fig. 4a, b). CTHRC1 expression was positively correlated with the CTHRC1-independent resistance core within all four sections, with Spearman ρ values of 0.281, 0.123, 0.172, and 0.434. Core program scores were also higher in CTHRC1-high than in CTHRC1-low spots in all four sections, with high-minus-low differences of 0.358, 0.752, 0.114, and 0.752, respectively. CTHRC1-high spots accounted for 21%, 3%, 25%, and 20% of the four sections (Fig. 4d), indicating that the CTHRC1-associated program was concentrated in focal spatial regions whose extent varied across sections.

CTHRC1-high neighborhoods also showed distinct immune and stromal features. M2-like TAM, CD8 cytotoxicity, CD8-related, T-cell exhaustion, and CAF programs were higher in CTHRC1-high regions, with median high-minus-low effects of 0.523, 0.313, 0.241, 0.189, and 0.111, respectively (Fig. 4c, e–h). The

exhaustion/CD8 composite showed a small negative shift (− 0.040), whereas the broader TAM and CAF-M2/CD8 composite scores showed little change. Thus, CTHRC1-high regions were not characterized by simple immune exclusion; CD8-associated and cytotoxic signals coexisted with CAF activation, M2-like macrophage programs, and T-cell exhaustion.

(c) Median CTHRC1-high minus CTHRC1-low neighborhood shifts in myeloid, stromal, and T-cell-related programs, with combined FDR q-values. (d) Section-level relationship between the within-section CTHRC1–resistance core Spearman correlation and the CTHRC1-high minus CTHRC1-low core program difference; point size represents the proportion of CTHRC1-high spots. (e–h) Distributions of M2-like TAM, CAF neighborhood, CD8 cytotoxicity, and T-cell exhaustion scores in CTHRC1-low and CTHRC1-high regions.

ADAMDEC1-associated macrophages exhibit a reproducible remodeling state associated with STAT1 regulation

Given the prominent myeloid features of the CTHRC1-associated spatial niche, we further analyzed the myeloid compartment in both single-cell datasets. S100A12-positive monocytes, SPP1-positive TAMs, and ADAMDEC1-associated macrophages were identified in both datasets and showed distinct marker expression patterns (Fig. 5a, b). Patient pseudobulk differential expression effects between ADAMDEC1-associated macrophages and S100A12-positive monocytes were positively correlated across the two datasets (Spearman $\rho = 0.64$). Among shared genes, 72.4% changed in the same direction, and 262 genes showed concordant FDR-supported changes in both datasets (Fig. 5c, d). Pathway enrichment analysis showed higher MHC-II antigen presentation and cholesterol efflux programs in the ADAMDEC1-associated state, together with lower inflammatory response, neutrophil chemotaxis, and cytoplasmic translation programs (Fig. 5e).

Focused pseudotime analysis placed S100A12-positive monocytes predominantly toward the early state, SPP1-positive TAMs in an intermediate region, and ADAMDEC1-associated macrophages toward the late state of the myeloid continuum (Fig. 5f). Dynamic expression analysis identified a late-stage transcriptional program containing STAT1 and other interferon response-related genes (Fig. 5g). Regulon prioritization ranked STAT1 first among regulators associated with the transition program, with IRF7 and STAT2 among the next-ranked candidates (Fig. 5h). STAT1 was therefore prioritized for subsequent receiver state-guided signaling analysis.

Receiver state-guided analysis prioritizes a JAM2–F11R–STAT1 axis associated with macrophage remodeling

We prioritized malignant-to-myeloid ligand–receptor pairs according to their association with the predefined STAT1 transition/ADAMDEC1 receiver state program. JAM2–F11R ranked first, with a fixed

TF/state explanation score of approximately 0.79, followed by JAM2–(ITGAV+ITGB1), GAS6–AXL, PTN–SDC3, PROS1–AXL, CSF1–CSF1R, and several collagen-related interactions (Fig. 6a).

Targeted in silico perturbation further linked F11R and STAT1 to the receiver state program. Virtual F11R knockout reduced the STAT1 regulon, STAT1 transition program, ADAMDEC1-associated macrophage state, and terminal state markers, whereas F11R overexpression produced changes in the opposite direction. STAT1 perturbation similarly altered the transition and ADAMDEC1-associated programs, with the largest effect observed for terminal state markers (Fig. 6b). The late-minus-early STAT1 transition AUC difference was positive in all five evaluable GSE193581 samples and in three of four evaluable GSE232237 samples (Fig. 6c).

We next examined spatial coupling among components of the candidate pathway. Positive spatial coupling was observed in all four ATC sections between the CTHRC1/JAM2 sender program and F11R (combined FDR = 0.0042), between F11R and the STAT1 transition program (FDR = 2.3 × 10^-6), and between the STAT1 transition program and the ADAMDEC1-associated macrophage state (FDR = 3.1 × 10^-22; Fig. 6d, e). Together, these analyses prioritized a JAM2–F11R–STAT1-linked signaling model associated with ADAMDEC1 macrophage remodeling in the CTHRC1-high malignant context (Fig. 6f).

CTHRC1-associated resistance features are linked to ICB nonresponse and perturbation-induced state shifts

In the two pretreatment melanoma ICB cohorts, the integrated CTHRC1-related feature score was higher in nonresponders, whereas raw CTHRC1 showed less separation between response groups (Fig. 7a). In cohort-adjusted logistic models, the integrated ICB feature score was associated with nonresponse (OR 2.17, 95% CI 1.22–3.86, FDR = 0.0097), as were CTHRC1 reversal burden (OR 2.90, FDR = 0.0012), AICR (OR 2.42, FDR = 0.0065), and EMT/ECM (OR 1.93, FDR = 0.0277). FAK/SRC and raw CTHRC1 were not significant after multiple testing correction (Fig. 7b). The integrated score yielded AUCs of 0.84 and 0.58 in GSE78220 and GSE91061, compared with 0.73 and 0.54 for raw CTHRC1, corresponding to ΔAUC values of + 0.11 and + 0.04, respectively (Fig. 7c). These ROC results were interpreted as within-cohort discrimination.

Virtual CTHRC1 knockout predicted negative median shifts across all eight resistance-related modules, ranging from − 0.36 for myCAF to − 0.66 for ECM remodeling (Fig. 7d). External perturbation datasets provided additional evidence that selected components of this transcriptional state were modifiable. In GSE248058, FAK inhibition with VS4718 produced modest changes in FAK/SRC and EMT/ECM programs at both the program and gene levels (Fig. 7e1, e2). In GSE211806, TGF-β induced coordinated gene- and signature-level changes that were reversed by galunisertib in PLC/PRF/5 and SNU-449 cells (Fig. 7e3, e4); the program-level induction and rescue effects remained significant after multiple testing correction (q = 0.010 for both).

(a) Distributions of standardized raw CTHRC1 expression and the integrated ICB feature score in responders and nonresponders from GSE78220 and GSE91061. (b) Cohort-adjusted associations of the integrated ICB feature score and individual transcriptional features with ICB nonresponse, shown as odds ratios with 95% confidence intervals and FDR values; bubble color represents log2 odds ratio and bubble area represents −log10 FDR. (c) Cohort-specific AUCs for standardized CTHRC1 and the integrated ICB feature score, with bootstrap 95% confidence intervals and ΔAUC relative to raw CTHRC1. (d) Sample-specific predicted changes in eight resistance-related modules after virtual CTHRC1 knockout across five malignant cell networks; the bar plot shows the median predicted change across samples. (e1) FAK/SRC and EMT/ECM program scores and FAK inhibitor-minus-vehicle changes after VS4718 treatment in mouse KP2 pancreatic ductal adenocarcinoma organoids. (e2) Gene-level transcriptional response to FAK inhibition. (e3) Gene-level effects of TGF-β induction and galunisertib-mediated rescue in PLC/PRF/5 and SNU-449 cells. (e4) TGF-β signature scores across control, TGF-β, galunisertib, and TGF-β + galunisertib conditions in the two cell lines.

Discussion

Immune checkpoint blockade has shown therapeutic activity in ATC, but resistance remains common and clinical benefit is heterogeneous [4–7]. Our integrative analyses prioritized CTHRC1 as a candidate linking ATC progression with ICB nonresponse and identified a broader CTHRC1-associated immune-resistant tumor state. Tumor ECM can arise from multiple cellular compartments [37], while CTHRC1-positive fibroblast programs have been associated with EMT [38], therapy resistance [39], tumor stemness [40], and ITGB3/FAK signaling [41]. CTHRC1-related programs have also been implicated in tumor invasion and immune evasion [42, 43]. In our spatial analysis, CTHRC1-high regions contained CAF and M2-like TAM programs together with CD8-associated cytotoxicity and T-cell exhaustion. This pattern suggests that immune resistance in ATC may not simply reflect immune exclusion, but rather impaired antitumor function within an immune-infiltrated microenvironment. This interpretation is consistent with previous evidence linking TGF-β/ECM programs to T-cell exclusion [8, 9], resistant CAF states [10, 11], and CAF-mediated restriction of CD8 + T-cell infiltration [12, 13].

Myeloid state analysis further identified a reproducible S100A12-positive monocyte–SPP1-positive TAM–ADAMDEC1-associated macrophage continuum. STAT1 ranked as the leading transition-associated regulator, consistent with previous evidence that STAT1 participates in transcriptional and metabolic regulation in tumor-associated macrophages [44]. Using this receiver state to prioritize malignant-to-myeloid communication identified JAM2–F11R as the top interaction. JAM2–F11R-mediated endothelial–macrophage communication has also been reported in hepatocellular carcinoma [45], providing biological precedent for this ligand–receptor pair in myeloid regulation. F11R/STAT1 perturbation, replication of the STAT1 transition program in an independent single-cell dataset, and spatial coupling across ATC sections further supported a JAM2–F11R–STAT1-linked model of macrophage state remodeling. Importantly, this receiver state-guided approach relates ligand–receptor communication to a reproducible myeloid phenotype rather than relying solely on the expression abundance of individual ligand–receptor pairs.

The ICB response and perturbation analyses further supported the potential therapeutic relevance of this resistance program. The integrated CTHRC1-related feature was more strongly associated with ICB nonresponse than CTHRC1 expression alone, suggesting that the broader transcriptional context may better capture immune resistance than a single marker. Virtual CTHRC1 knockout predicted coordinated reductions in multiple resistance-related programs, while external perturbation data supported the reversibility of the TGF-β-related component [31]. These findings suggest that CTHRC1 may represent a potential intervention point within the immune-resistant ATC microenvironment, whereas JAM2–F11R–STAT1-associated macrophage remodeling provides a candidate intercellular mechanism contributing to this state.

Limitations

Several limitations should be acknowledged. This study integrated multiple independent ATC datasets, including bulk, single-cell, and spatial transcriptomic data, providing cross-dataset support for the major findings. Because ATC-specific immunotherapy cohorts were unavailable, two independent melanoma ICB cohorts were used to assess whether the identified resistance features were also associated with ICB nonresponse; however, their predictive value in ATC requires further validation. Finally, the identification of CTHRC1 as a candidate target and the JAM2–F11R–STAT1-associated pathway was based on computational analyses of publicly available datasets and therefore requires further experimental validation in ATC models.

Conclusions

This study integrated multiple ATC bulk transcriptomic cohorts with single-cell and spatial transcriptomic datasets to identify a CTHRC1-associated immune resistance niche in ATC. Cross-cohort transcriptomic analyses, independent single-cell replication, spatial coupling, ICB response analyses, and in silico perturbation supported the biological relevance of CTHRC1, the ADAMDEC1-associated macrophage state, and the candidate JAM2–F11R–STAT1 signaling axis in ATC immune resistance. These findings suggest that CTHRC1 may represent a potential therapeutic target for overcoming immune resistance in ATC.

Declarations

Ethics approval and consent to participate

Not applicable. This study used publicly available data.

Consent for publication

Not applicable.

Availability of data and materials

All datasets analyzed in this study are publicly available through the NCBI Gene Expression Omnibus (GEO). The accession numbers and direct access links are provided below:

GSE29265: https://www.ncbi.nlm.nih.gov/geo/query/acc.cgi?acc=GSE29265
GSE33630: https://www.ncbi.nlm.nih.gov/geo/query/acc.cgi?acc=GSE33630
GSE53072: https://www.ncbi.nlm.nih.gov/geo/query/acc.cgi?acc=GSE53072
GSE65144: https://www.ncbi.nlm.nih.gov/geo/query/acc.cgi?acc=GSE65144
GSE76039: https://www.ncbi.nlm.nih.gov/geo/query/acc.cgi?acc=GSE76039
GSE9115: https://www.ncbi.nlm.nih.gov/geo/query/acc.cgi?acc=GSE9115
GSE27155: https://www.ncbi.nlm.nih.gov/geo/query/acc.cgi?acc=GSE27155
GSE193581: https://www.ncbi.nlm.nih.gov/geo/query/acc.cgi?acc=GSE193581
GSE232237: https://www.ncbi.nlm.nih.gov/geo/query/acc.cgi?acc=GSE232237
GSE250521: https://www.ncbi.nlm.nih.gov/geo/query/acc.cgi?acc=GSE250521
GSE78220: https://www.ncbi.nlm.nih.gov/geo/query/acc.cgi?acc=GSE78220
GSE91061: https://www.ncbi.nlm.nih.gov/geo/query/acc.cgi?acc=GSE91061
GSE248058: https://www.ncbi.nlm.nih.gov/geo/query/acc.cgi?acc=GSE248058
GSE211806: https://www.ncbi.nlm.nih.gov/geo/query/acc.cgi?acc=GSE211806

Competing interests

The authors have declared that no competing interests exist.

Funding

No specific funding was received for this study.

Clinical trial number

Not applicable.

Authors' contributions

XW conceived and designed the study, performed the bioinformatic analyses, interpreted the results, prepared the figures, and drafted the manuscript. BZ contributed to the study conception and design, supervised the study, interpreted the results, and critically revised the manuscript. KY and PD contributed to data curation, result verification, and manuscript review and editing. All authors read and approved the final manuscript.

Acknowledgements

Not applicable.

References

1. Cabanillas ME, McFadden DG, Durante C. Thyroid cancer. Lancet. 2016;388:2783–95. https://doi.org/10.1016/S0140-6736(16)30172-6.
2. Maniakas A, Dadu R, Busaidy NL, Wang JR, Ferrarotto R, Lu C, et al. Evaluation of Overall Survival in Patients With Anaplastic Thyroid Carcinoma, 2000–2019. JAMA Oncol. 2020;6:1397–404. https://doi.org/10.1001/jamaoncol.2020.3362.
3. Subbiah V, Kreitman RJ, Wainberg ZA, Cho JY, Schellens JHM, Soria JC, et al. Dabrafenib plus trametinib in patients with BRAF V600E-mutant anaplastic thyroid cancer: updated analysis from the phase II ROAR basket study. Ann Oncol. 2022;33:406–15. https://doi.org/10.1016/j.annonc.2021.12.014.
4. Capdevila J, Wirth LJ, Ernst T, Ponce Aix S, Lin CC, Ramlau R, et al. PD-1 Blockade in Anaplastic Thyroid Carcinoma. J Clin Oncol. 2020;38:2620–7. https://doi.org/10.1200/JCO.19.02727.
5. Hatashima A, Archambeau B, Armbruster H, Xu M, Shah M, Konda B, et al. An Evaluation of Clinical Efficacy of Immune Checkpoint Inhibitors for Patients with Anaplastic Thyroid Carcinoma. Thyroid. 2022;32:926–36. https://doi.org/10.1089/thy.2022.0073.
6. Sehgal K, Pappa T, Shin KY, Schiantarelli J, Liu M, Ricker C, et al. Dual Immune Checkpoint Inhibition in Patients With Aggressive Thyroid Carcinoma: A Phase 2 Nonrandomized Clinical Trial. JAMA Oncol. 2024;10:1663–71. https://doi.org/10.1001/jamaoncol.2024.4019.
7. Cabanillas ME, Dadu R, Ferrarotto R, Gule-Monroe M, Liu S, Fellman B, et al. Anti-Programmed Death Ligand 1 Plus Targeted Therapy in Anaplastic Thyroid Carcinoma: A Nonrandomized Clinical Trial. JAMA Oncol. 2024;10:1672–80. https://doi.org/10.1001/jamaoncol.2024.4729.
8. Mariathasan S, Turley SJ, Nickles D, Castiglioni A, Yuen K, Wang Y, et al. TGFβ attenuates tumour response to PD-L1 blockade by contributing to exclusion of T cells. Nature. 2018;554:544–8. https://doi.org/10.1038/nature25501.
9. Chakravarthy A, Khan L, Bensler NP, Bose P, De Carvalho DD. TGF-β-associated extracellular matrix genes link cancer-associated fibroblasts to immune evasion and immunotherapy failure. Nat Commun. 2018;9:4692. https://doi.org/10.1038/s41467-018-06654-8.
10. Kieffer Y, Hocine HR, Gentric G, Pelon F, Bernard C, Bourachot B, et al. Single-Cell Analysis Reveals Fibroblast Clusters Linked to Immunotherapy Resistance in Cancer. Cancer Discov. 2020;10:1330–51. https://doi.org/10.1158/2159-8290.CD-19-1384.
11. Dominguez CX, Müller S, Keerthivasan S, Koeppen H, Hung J, Gierke S, et al. Single-Cell RNA Sequencing Reveals Stromal Evolution into LRRC15 + Myofibroblasts as a Determinant of Patient Response to Cancer Immunotherapy. Cancer Discov. 2020;10:232–53. https://doi.org/10.1158/2159-8290.CD-19-0644.

12. Jenkins L, Jungwirth U, Avgustinova A, Iravani M, Mills A, Haider S, et al. Cancer-Associated Fibroblasts Suppress CD8 + T-cell Infiltration and Confer Resistance to Immune-Checkpoint Blockade. Cancer Res. 2022;82:2904–17. https://doi.org/10.1158/0008-5472.CAN-21-4141.
13. Lu X, Gou Z, Chen H, Li L, Chen F, Bao C, et al. Extracellular matrix cancer-associated fibroblasts promote stromal fibrosis and immune exclusion in triple-negative breast cancer. J Pathol. 2025;265:385–99. https://doi.org/10.1002/path.6395.
14. Pich-Bavastro C, Yerly L, Di Domizio J, Tissot-Renaud S, Gilliet M, Kuonen F. Activin A-Mediated Polarization of Cancer-Associated Fibroblasts and Macrophages Confers Resistance to Checkpoint Immunotherapy in Skin Cancer. Clin Cancer Res. 2023;29:3498–513. https://doi.org/10.1158/1078-0432.CCR-23-0219.
15. Jiang H, Hegde S, Knolhoff BL, Zhu Y, Herndon JM, Meyer MA, et al. Targeting focal adhesion kinase renders pancreatic cancers responsive to checkpoint immunotherapy. Nat Med. 2016;22:851–60. https://doi.org/10.1038/nm.4123.
16. Byun H, Lee HS, Song YS, Park YJ. Transcriptome of Anaplastic Thyroid Cancer Reveals Two Molecular Subtypes with Distinct Tumor Microenvironment and Prognosis. Thyroid. 2025;35:367–78. https://doi.org/10.1089/thy.2024.0266.
17. Zeng PYF, Prokopec SD, Lai SY, Pinto N, Chan-Seng-Yue MA, Clifton-Bligh R, et al. The genomic and evolutionary landscapes of anaplastic thyroid carcinoma. Cell Rep. 2024;43:113826. https://doi.org/10.1016/j.celrep.2024.113826.
18. Lu L, Wang JR, Henderson YC, Bai S, Yang J, Hu M, et al. Anaplastic transformation in thyroid cancer revealed by single-cell transcriptomics. J Clin Invest. 2023;133:e169653. https://doi.org/10.1172/JCI169653.
19. Feng C, Tao Y, Yu C, Wang L, Liu X, Cao Y. Integrative single-cell transcriptome analysis reveals immune suppressive landscape in the anaplastic thyroid cancer. Cancer Gene Ther. 2023;30:1598–609. https://doi.org/10.1038/s41417-023-00663-6.
20. Han PZ, Ye WD, Yu PC, Tan LC, Shi X, Chen XF, et al. A distinct tumor microenvironment makes anaplastic thyroid cancer more lethal but immunotherapy sensitive than papillary thyroid cancer. JCI Insight. 2024;9:e173712. https://doi.org/10.1172/jci.insight.173712.
21. Ruan X, Tao M, Dong Y, Hu L, Xu G, Hu C, et al. Persistent pre-exhausted CD8 + T cells shape the tumor immune microenvironment in anaplastic thyroid cancer. Endocr Relat Cancer. 2025;32:e240169. https://doi.org/10.1530/ERC-24-0169.
22. Liao T, Zeng Y, Xu W, Shi X, Shen C, Du Y, et al. A spatially resolved transcriptome landscape during thyroid cancer progression. Cell Rep Med. 2025;6:102043. https://doi.org/10.1016/j.xcrm.2025.102043.
23. Loberg MA, Xu GJ, Chen SC, Chen HC, Wahoski CC, Caroland KP, et al. An integrated single-cell and spatial transcriptomic atlas of thyroid cancer progression identifies prognostic fibroblast subpopulations. JCI Insight. 2026;11:e191990. https://doi.org/10.1172/jci.insight.191990.

24. Haq F, Bychkov A, Mete O, Jeon S, Jung CK. Identification of Specific Biomarkers for Anaplastic Thyroid Carcinoma Through Spatial Transcriptomic and Immunohistochemical Profiling. Endocr Pathol. 2025;36:14. https://doi.org/10.1007/s12022-025-09858-z.
25. Xia J, Shi Y, Chen X. New insights into the mechanisms of the extracellular matrix and its therapeutic potential in anaplastic thyroid carcinoma. Sci Rep. 2024;14:20977. https://doi.org/10.1038/s41598-024-72020-y.
26. Pan Z, Xu T, Bao L, Hu X, Jin T, Chen J, et al. CREB3L1 promotes tumor growth and metastasis of anaplastic thyroid carcinoma by remodeling the tumor microenvironment. Mol Cancer. 2022;21:190. https://doi.org/10.1186/s12943-022-01658-x.
27. Hugo W, Zaretsky JM, Sun L, Song C, Moreno BH, Hu-Lieskovan S, et al. Genomic and Transcriptomic Features of Response to Anti-PD-1 Therapy in Metastatic Melanoma. Cell. 2016;165:35–44. https://doi.org/10.1016/j.cell.2016.02.065.
28. Riaz N, Havel JJ, Makarov V, Desrichard A, Urba WJ, Sims JS, et al. Tumor and Microenvironment Evolution during Immunotherapy with Nivolumab. Cell. 2017;171. https://doi.org/10.1016/j.cell.2017.09.028. 934 – 49.e16.
29. Lee SE, Park S, Yi S, Choi NR, Lim MA, Chang JW, et al. Unraveling the role of the mitochondrial one-carbon pathway in undifferentiated thyroid cancer by multi-omics analyses. Nat Commun. 2024;15:1163. https://doi.org/10.1038/s41467-024-45366-0.
30. Liu X, Baer JM, Stone ML, Knolhoff BL, Hogg GD, Turner MC, et al. Stromal reprogramming overcomes resistance to RAS-MAPK inhibition to improve pancreas cancer responses to cytotoxic and immune therapy. Sci Transl Med. 2024;16:eado2402. https://doi.org/10.1126/scitranslmed.ado2402.
31. Desoteux M, Maillot B, Bévant K, Ferlier T, Leroux R, Angenard G, et al. Transcriptomic evidence for tumor-specific beneficial or adverse effects of TGFβ pathway inhibition on the prognosis of patients with liver cancer. FEBS Open Bio. 2023;13:1278–90. https://doi.org/10.1002/2211-5463.13647.
32. Ritchie ME, Phipson B, Wu D, Hu Y, Law CW, Shi W, et al. limma powers differential expression analyses for RNA-sequencing and microarray studies. Nucleic Acids Res. 2015;43:e47. https://doi.org/10.1093/nar/gkv007.
33. Stuart T, Butler A, Hoffman P, Hafemeister C, Papalexi E, Mauck WM, et al. Comprehensive Integration of Single-Cell Data. Cell. 2019;177. https://doi.org/10.1016/j.cell.2019.05.031. 1888 – 902.e21.
34. Browaeys R, Saelens W, Saeys Y. NicheNet: modeling intercellular communication by linking ligands to target genes. Nat Methods. 2020;17:159–62. https://doi.org/10.1038/s41592-019-0667-5.
35. Fischer DS, Schaar AC, Theis FJ. Modeling intercellular communication in tissues using spatial graphs of cells. Nat Biotechnol. 2023;41:332–6. https://doi.org/10.1038/s41587-022-01467-z.
36. Osorio D, Zhong Y, Li G, Xu Q, Yang Y, Tian Y et al. scTenifoldKnk: An efficient virtual knockout tool for gene function predictions via single-cell gene regulatory network perturbation. Patterns (N Y). 2022; 3: 100434. https://doi.org/10.1016/j.patter.2022.100434

37. Lee HJ, Park SW, Lee JH, Chang SY, Oh SM, Mun S, et al. Differential cellular origins of the extracellular matrix of tumor and normal tissues according to colorectal cancer subtypes. Br J Cancer. 2025;132:770–82. https://doi.org/10.1038/s41416-025-02964-z.
38. Lu Y, Chen Y, Wang Z, Shen H, Xu L, Huang C, et al. Single-cell and spatial transcriptome profiling reveal CTHRC1 + fibroblasts promote EMT through WNT5A signaling in colorectal cancer. J Transl Med. 2025;23:282. https://doi.org/10.1186/s12967-025-06236-5.
39. Zhang C, Zhou W, Xu H, Xu J, Li J, Liu X, et al. Cancer-associated fibroblasts promote EGFR-TKI resistance via the CTHRC1/glycolysis/H3K18la positive feedback loop. Oncogene. 2025;44:1400–14. https://doi.org/10.1038/s41388-025-03318-y.
40. Huang H, Peng W, Zhou Q, Zhao Y, Liu L, Cui H, et al. Senescent fibroblasts secrete CTHRC1 to promote cancer stemness in hepatocellular carcinoma. Cell Commun Signal. 2025;23:379. https://doi.org/10.1186/s12964-025-02369-8.
41. Bian Y, Chang X, Hu X, Li B, Song Y, Hu Z, et al. Exosomal CTHRC1 from cancer-associated fibroblasts facilitates endometrial cancer progression via ITGB3/FAK signaling pathway. Heliyon. 2024;10:e35727. https://doi.org/10.1016/j.heliyon.2024.e35727.
42. Wan H, Ling Z, Xie Y, Jiang H, Ruan Z, Yang D, et al. Single-cell and transcriptome analyses revealed CTHRC1 a potential therapeutic target mediating invasion and tumor microenvironment in TNBC: experimental validation. Front Immunol. 2025;16:1534981. https://doi.org/10.3389/fimmu.2025.1534981.
43. Chen Q, Wang H, Liu Q, Luo C. CTHRC1: a key player in colorectal cancer progression and immune evasion. Front Immunol. 2025;16:1579661. https://doi.org/10.3389/fimmu.2025.1579661.
44. Huffaker TB, Ekiz HA, Barba C, Lee SH, Runtsch MC, Nelson MC, et al. A Stat1 bound enhancer promotes Nampt expression and function within tumor associated macrophages. Nat Commun. 2021;12:2620. https://doi.org/10.1038/s41467-021-22923-5.
45. Hu Z, Yue P, Yuan M, Zhang Z, Li Q, Yang T, et al. Stress accelerates hepatocellular carcinoma progression via a gut microbial-metabolite axis. Front Immunol. 2026;17:1790214. https://doi.org/10.3389/fimmu.2026.1790214.

Figures

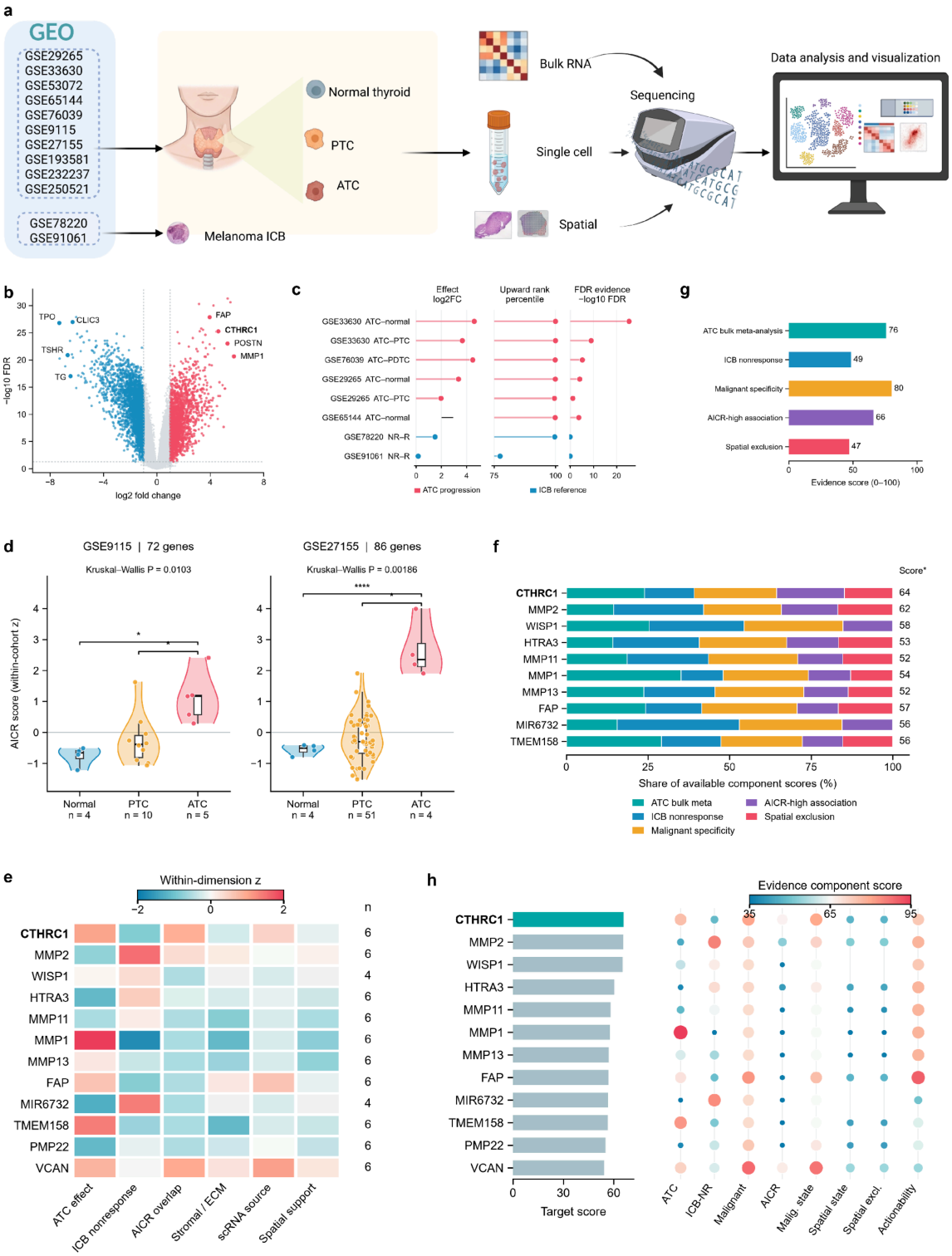


Figure 1

Multi-cohort prioritization of CTHRC1 across ATC progression and ICB nonresponse. (a) Study design and core public datasets used for bulk transcriptomic, single-cell, spatial, and ICB response analyses. (b) Representative differential expression analysis of ATC versus normal thyroid tissue in GSE33630, highlighting CTHRC1. (c) Cross-dataset evidence for CTHRC1 across ATC progression-related and ICB nonresponse contrasts, showing effect size (log2FC), upward rank percentile, and FDR evidence (−log10

FDR). (d) Within-cohort standardized AICR scores across normal thyroid, PTC, and ATC samples in GSE9115 and GSE27155. (e) Candidate gene evidence matrix summarizing ATC effect, ICB nonresponse, AICR overlap, stromal/ECM association, single-cell source, and spatial support. (f) Relative contributions of the five scoring components to the integrated scores of the leading candidates. (g) Evidence component scores for CTHRC1 across ATC bulk meta-analysis, ICB nonresponse, malignant specificity, AICR-high association, and spatial exclusion. (h) Integrated target scores and broader evidence component profiles of the leading candidates.

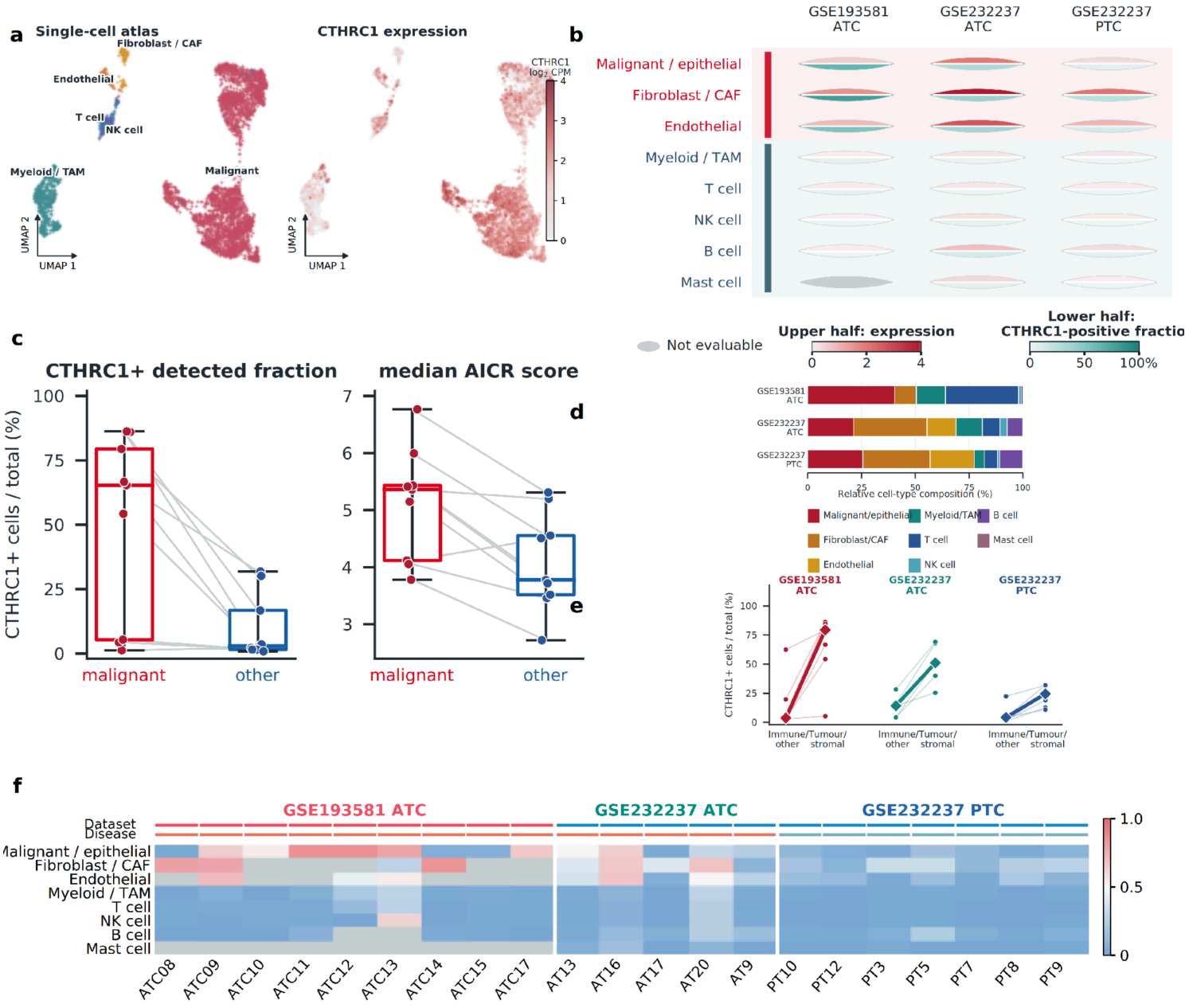


Figure 2

Cellular distribution of CTHRC1 across single-cell datasets. (a) Single-cell atlas and CTHRC1 expression in GSE193581 and GSE232237. (b) Split violin plots of CTHRC1 expression and CTHRC1-positive fractions across major cell populations in GSE193581 ATC, GSE232237 ATC, and GSE232237 PTC; the

upper half represents expression level and the lower half represents the CTHRC1-positive fraction. (c) Within-patient comparisons of CTHRC1-positive fractions and median AICR scores between malignant/epithelial cells and the remaining cell populations. (d) Relative cell type composition of the CTHRC1-positive cell pool across the three dataset/disease groups.
(e) Within-patient comparison of tumor/stromal and immune/other CTHRC1 source summaries across the three groups. (f) Patient-level heatmap of CTHRC1-positive fractions across major cell populations; gray indicates non-evaluable combinations.

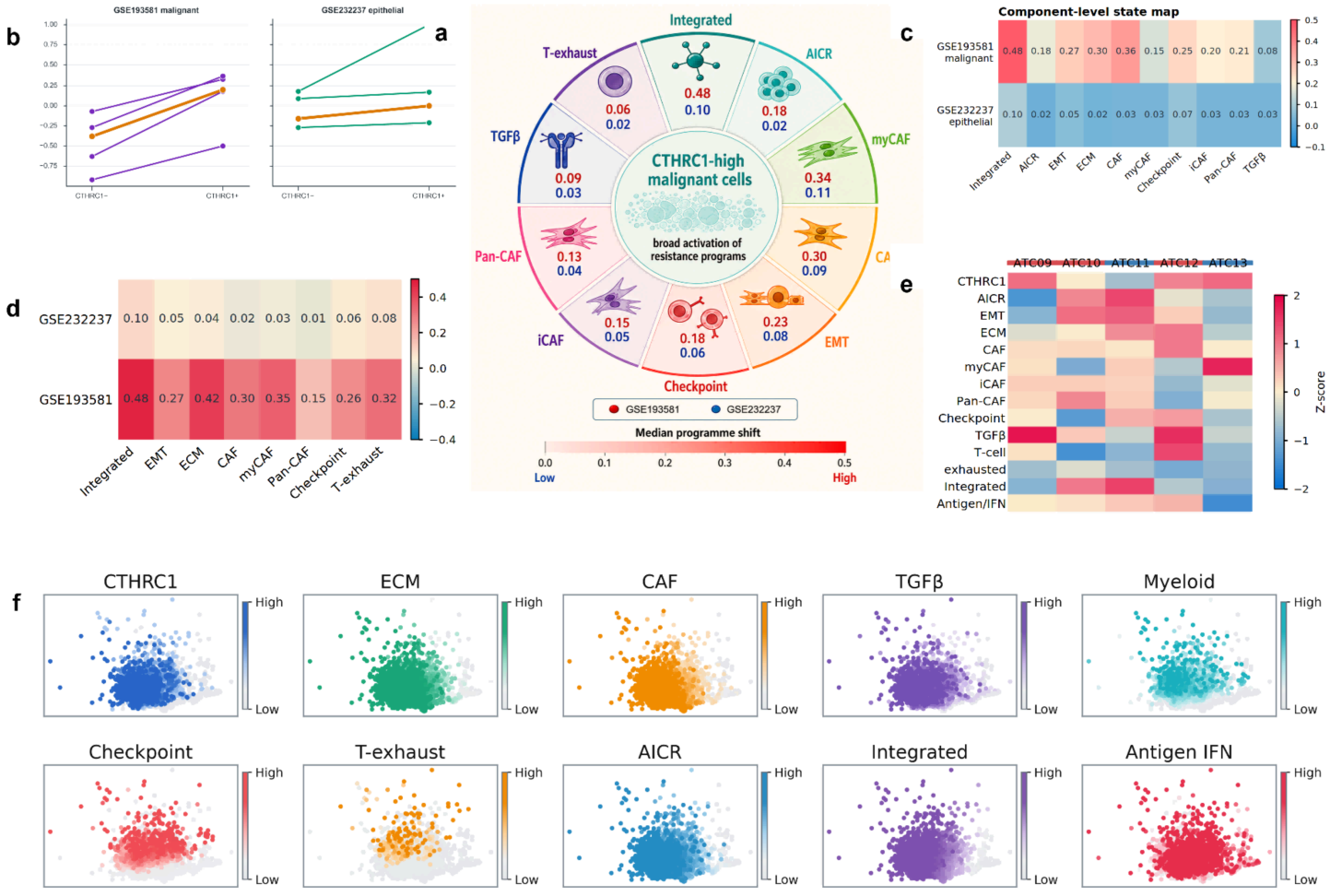


Figure 3

Resistance-associated transcriptional programs in CTHRC1-positive malignant/epithelial cells. (a) Radial summary of median CTHRC1-positive minus CTHRC1-negative shifts in the integrated score and individual resistance-related programs in GSE193581 and GSE232237. (b) Within-patient changes in the CTHRC1-independent integrated resistance score between CTHRC1-negative and CTHRC1-positive malignant/epithelial cells. (c) Component-level summary of median within-patient shifts across resistance-related transcriptional programs in the two single-cell datasets. (d) Cross-dataset heatmap of selected resistance program shifts between CTHRC1-positive and CTHRC1-negative malignant/epithelial

cells. (e) Patient-level pseudobulk profiles of CTHRC1 and resistance-related transcriptional features. (f) Representative single-cell activity maps of CTHRC1 and selected resistance-related programs. CTHRC1 was excluded from the AICR and integrated resistance scores used for CTHRC1 state comparisons. Color scales in panel F are specific to each transcriptional program.

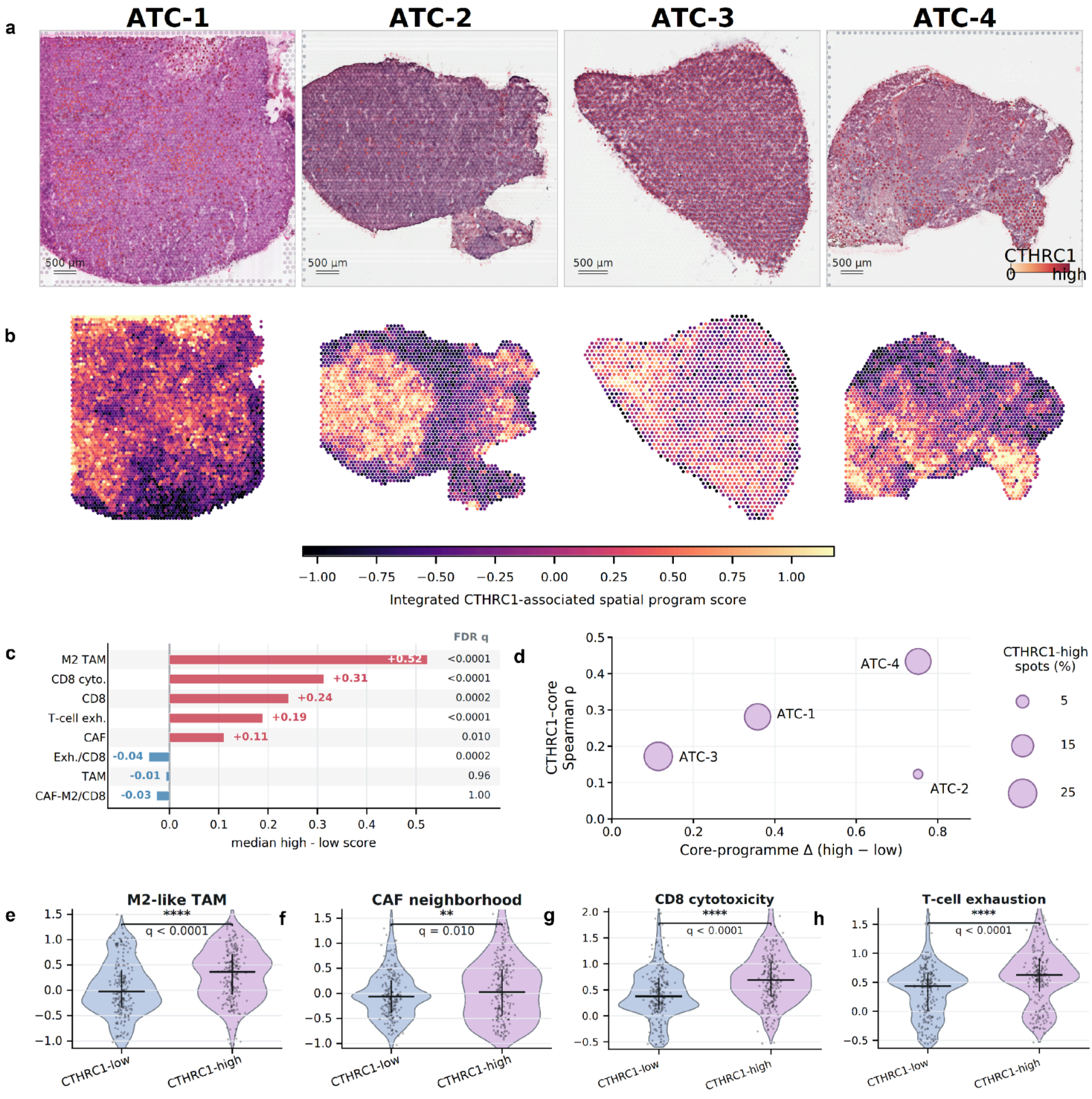


Figure 4

Spatial organization of the CTHRC1-associated resistance niche. (a) H&E images of four ATC Visium sections with spatial CTHRC1 expression overlaid. (b) Spatial distribution of the integrated CTHRC1-

associated program score across the four sections.
(c) Median CTHRC1-high minus CTHRC1-low neighborhood shifts in myeloid, stromal, and T-cell-related programs, with combined FDR q-values. (d) Section-level relationship between the within-section CTHRC1–resistance core Spearman correlation and the CTHRC1-high minus CTHRC1-low core program difference; point size represents the proportion of CTHRC1-high spots. (e–h) Distributions of M2-like TAM, CAF neighborhood, CD8 cytotoxicity, and T-cell exhaustion scores in CTHRC1-low and CTHRC1-high regions.

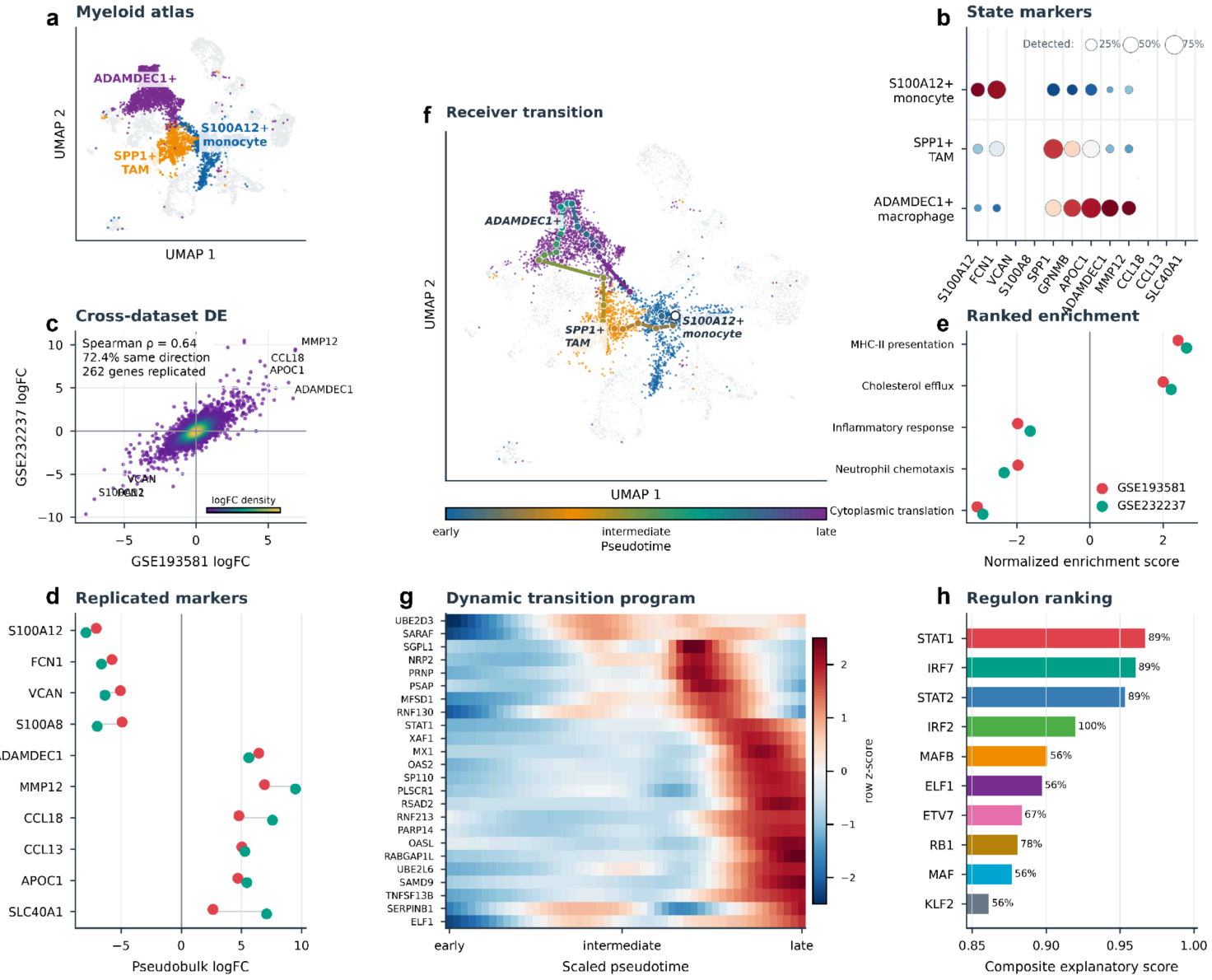


Figure 5

Cross-dataset characterization of an ADAMDEC1-associated macrophage remodeling state. (a) Myeloid cell atlas highlighting S100A12-positive monocytes, SPP1-positive TAMs, and ADAMDEC1-associated macrophages. (b) Expression of representative markers across the three myeloid states; dot size represents the fraction of cells expressing each gene. (c) Cross-dataset concordance of patient pseudobulk differential expression effects between ADAMDEC1-associated macrophages and S100A12-

positive monocytes. (d) Representative genes showing concordant state-associated effects in GSE193581 and GSE232237. (e) Ranked pathway enrichment associated with the ADAMDEC1 macrophage state across the two datasets. (f) Focused pseudotime trajectory spanning S100A12-positive monocytes, SPP1-positive TAMs, and ADAMDEC1-associated macrophages. (g) Dynamic transcriptional program along scaled pseudotime. (h) Regulon ranking associated with the myeloid state transition program, with STAT1 ranked first.



Figure 6

Receiver state-guided prioritization of a JAM2–F11R–STAT1 axis associated with macrophage remodeling. (a) Ranking of malignant-to-myeloid ligand–receptor pairs according to their association with the predefined STAT1 transition/ADAMDEC1 receiver state program; JAM2–F11R ranked first. (b) Targeted in silico knockout and overexpression of F11R and STAT1, summarized across the STAT1 regulon, STAT1 transition program, ADAMDEC1-associated macrophage state, terminal state markers, and root state markers. (c) Late-minus-early STAT1 transition AUC differences across evaluable samples

in GSE193581 and GSE232237. (d) Four-section Stouffer meta-analysis of spatial coupling between the CTHRC1/JAM2 sender program and F11R, F11R and the STAT1 transition program, and the STAT1 transition program and the ADAMDEC1-associated macrophage state. (e) Representative spatial maps from ATC-1 and ATC-4 showing the CTHRC1/JAM2 sender program, F11R receptor signal, STAT1 transition program, and ADAMDEC1-associated macrophage state. (f) Schematic of the candidate JAM2–F11R–STAT1 axis linking the CTHRC1-high malignant cell context with a STAT1-centered transcriptional program and the ADAMDEC1-associated macrophage state.

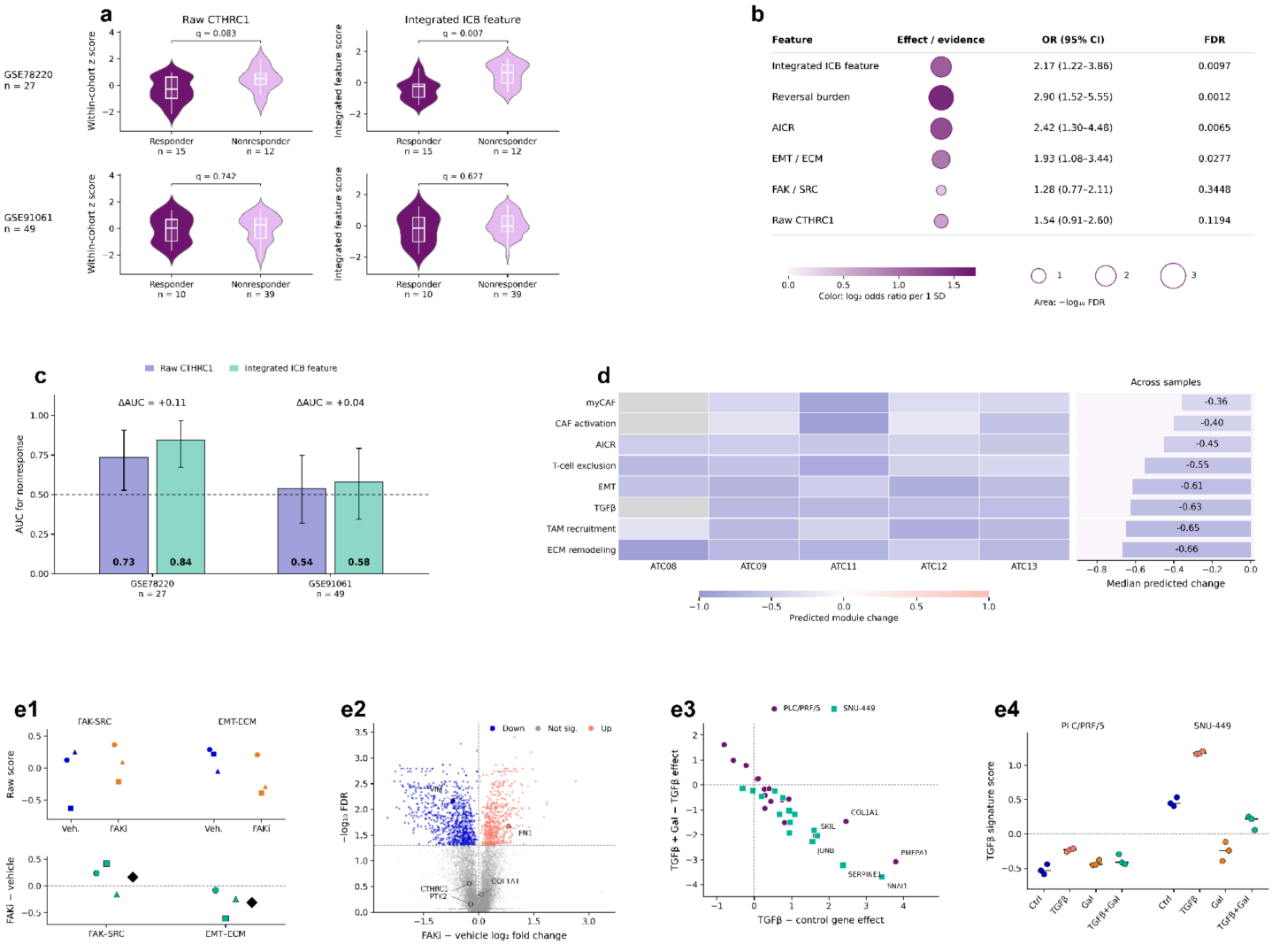


Figure 7

Association of CTHRC1-related resistance features with ICB nonresponse and perturbation-induced transcriptional changes.
(a) Distributions of standardized raw CTHRC1 expression and the integrated ICB feature score in responders and nonresponders from GSE78220 and GSE91061. (b) Cohort-adjusted associations of the integrated ICB feature score and individual transcriptional features with ICB nonresponse, shown as

odds ratios with 95% confidence intervals and FDR values; bubble color represents log2 odds ratio and bubble area represents −log10 FDR. (c) Cohort-specific AUCs for standardized CTHRC1 and the integrated ICB feature score, with bootstrap 95% confidence intervals and ΔAUC relative to raw CTHRC1. (d) Sample-specific predicted changes in eight resistance-related modules after virtual CTHRC1 knockout across five malignant cell networks; the bar plot shows the median predicted change across samples. (e1) FAK/SRC and EMT/ECM program scores and FAK inhibitor-minus-vehicle changes after VS4718 treatment in mouse KP2 pancreatic ductal adenocarcinoma organoids. (e2) Gene-level transcriptional response to FAK inhibition. (e3) Gene-level effects of TGF-β induction and galunisertib-mediated rescue in PLC/PRF/5 and SNU-449 cells. (e4) TGF-β signature scores across control, TGF-β, galunisertib, and TGF-β + galunisertib conditions in the two cell lines.